



Towards Size-Controlled Deposition of Palladium Nanoparticles from Polyoxometalate Precursors: An Electrochemical Scanning Tunneling Microscopy Study

Nicolas Bock⁺,^[a] Astrid De Clercq⁺,^[a] Lukas Seidl,^[b] Tim Kratky,^[a] Tian Ma,^[c] Sebastian Günther,^[a] Ulrich Kortz,^[c] Ueli Heiz,^[a] and Friedrich Esch^{*[a]}

We present a novel *in situ* electrochemical approach to deposit small size-controlled palladium(0) clusters from 12-Pd^{II}-oxometalate precursors. These clusters are formed through the reductive surface polarization of a Au(111) support. Electrochemical scanning tunneling microscopy (EC-STM) reveals that the electrochemical reduction occurs at much lower potentials than that for simple Pd salt solutions. The resulting particles are one atomic layer high and show a narrow size distribution. Precursor mass transport limitations and preconditioning of the

solid-liquid interface at low potentials influence the obtained morphology. In particular, a concomitant reduction mechanism via formation of molecular hydrogen is discussed. The deposited clusters show the typical behavior of small metallic Pd islands in EC-STM: The apparent cluster height increases reversibly when lowering the potential close to the onset of hydrogen evolution, which is attributed to hydrogen adsorption.

1. Introduction

In the search for an efficient production of alternative green mobile energy carriers such as hydrogen and other synthetic solar fuels, a fundamental understanding of their catalytic synthesis at the solid-liquid interface is crucial. Platinum Group Metal (PGM) alloys remain the most active catalytic material in many of these applications and moreover they seem to be inevitable in neutral solutions, which could give benefits in terms of durability compared to the standard harsh acidic or alkaline conditions.^[1] As their high cost inhibits widespread commercialization, an effective strategy has been to reduce metal loading by finely dispersing it in the form of nanoparticles.^[2] The particles' size can be controlled down to atomic precision. For nanometer-sized metal clusters, this opens

up the possibility to steer their morphological and electronic properties for a desired reactivity, exploiting quantum effects in the non-scalable size regime. Such atom-by-atom size dependences have been intensely studied at the solid-gas interface, demonstrating that single atom differences can indeed cause significant variations in catalyst performance.^[3] While size-selected clusters can be prepared in vacuum systems by laser ablation or magnetron sputtering and subsequent mass selection, an extension of these studies to the solid-liquid interface has been hampered by the limitations of a sample transfer from vacuum into liquid under atmospheric conditions. Nevertheless, beneficial turnover rates per atom were reported for some specific sizes and reactions in liquid.^[3–6]

An alternative strategy is the wet-chemical deposition of metal complexes with an exact number of noble metal atoms in a surrounding stabilizing ligand shell. Examples for such an approach are the impregnation of a support by platinum octanethiolate^[7] or polyoxopalladates(II) (POPs) and the subsequent calcination and reduction towards the active metallic state.^[8] POPs have also been investigated as molecular precursors for heterogeneous catalysts through incorporation into metal organic frameworks (MOFs).^[9] POP-based heterogeneous catalysts with a well-defined size distribution show promising catalytic properties ranging from cross-coupling reactions^[10,11] to hydrogenations.^[8] The calcination step, however, leads to an unwanted increase in size and therefore the unique potential of these complexes as precursors for size-selected clusters remains largely unexplored.

Otherwise, direct wet-chemical synthesis of metal particles in the liquid phase^[12] can be achieved by the dendrimer^[13] or micelle-encapsulation^[14] technique. Here, Imaoka et al. demonstrated that so-formed Pt₁₂ clusters on a carbon support show a more than 2-fold increase in reactivity compared to Pt₁₃ in the oxygen reduction reaction (ORR).^[13] However, even if these wet-

[a] N. Bock,⁺ Dr. A. De Clercq,⁺ T. Kratky, Prof. Dr. S. Günther, Prof. Dr. U. Heiz, Dr. F. Esch
Catalysis Research Center and Chemistry Department
Technical University of Munich
Lichtenbergstr. 4, 85748 Garching, Germany
E-mail: friedrich.esch@tum.de

[b] Dr. L. Seidl
Department Mobility, Energy & Environment
Swiss Federal Laboratories for Materials Science and Technology
Überlandstrasse 129, 8600 Dübendorf, Switzerland

[c] Dr. T. Ma, Prof. Dr. U. Kortz
Department of Life Sciences and Chemistry
Jacobs University
Campus Ring 1, 28759 Bremen, Germany

⁺ These authors contributed equally to this work

 Supporting information for this article is available on the WWW under
<https://doi.org/10.1002/celc.202100131>

 © 2021 The Authors. ChemElectroChem published by Wiley-VCH GmbH. This is an open access article under the terms of the Creative Commons Attribution Non-Commercial NoDerivs License, which permits use and distribution in any medium, provided the original work is properly cited, the use is non-commercial and no modifications or adaptations are made.

chemical methods pave the way for a deposition beyond flat surfaces, e.g. onto powders and into porous supports, they encounter specific limitations related to the removal of the protective ligand shell and require a compromise between activation and agglomeration.^[15]

In this work, we explore instead a different, electrochemical route, to dissociate and deposit POP precursors to form metallic Pd clusters. The family of discrete POPs shows distinct stoichiometries – POPs with $n=12$ up to 84 could be prepared^[16] and are sufficiently labile to be decomposed electrochemically, or alternatively by pH changes or contact with molecular hydrogen.^[8,17,18,19,20,21] We decided to study in particular the POP with an “open-shell” structure, $[\text{SrPd}_{12}\text{O}_6(\text{OH})_3(\text{PhAsO}_3)_6(\text{OAc})_3]^{4-}$ (SrPd_{12} , structure see Figure S1), which we reduced directly at the solid-liquid interface, obtaining well-defined palladium(0) cluster sizes. Synthesis and structural details can be found in Yang et al.^[17] This “open-shell” polyanion SrPd_{12} was selected due to its presence of acetate and phenylarsonate ligands, the former being sterically less demanding than the latter. This structural feature is expected to facilitate electron transfer in the reduction process, as compared to for example the highly symmetrical, closed-shell CaPd_{12} nanocube or BaPd_{15} nanostar with exclusively phenylarsonate ligands.^[17]

Other POPs and Pd^{II} -containing heteropolytungstates have already been used to electrodeposit extended Pd films that showed high stability, fast hydrogen sorption/desorption kinetics, and high electrocatalytic activity in reactions such as hydrazine and alcohol oxidation.^[18,19,20,21] However, the unique microstructure of these Pd films has neither been studied in detail at the nanoscale nor optimized. Other 3d transition metal-containing POMs, such as Mn^{II} -containing heteropolyanions, were successfully deposited and characterized at the nanoscale with intact ligand shell^[22] and with stripped ligands,^[23] but without reducing the oxygen framework prior to the catalytic application.

Here, we use a combination of electrochemical and microscopic techniques to determine the possible deposition mechanisms and their effect on the particle morphology. Electrochemical Scanning Tunneling Microscopy (EC-STM) has already proven to be a powerful method to investigate *in situ*, at the local scale and under potential control the deposition of small Pd particles from simple salt solutions and their properties.^[24-29] As supports, both reconstructed $\text{Au}(111)-(22 \times \sqrt{3})$ and unreconstructed $\text{Au}(111)-(1 \times 1)$ surfaces were used, as well as Highly Oriented Pyrolytic Graphite (HOPG). Pd on Au supports is known to be active in the hydrogen evolution reaction (HER). Since the boundary between Au and Pd represents the most active centers, a controlled fine Pd dispersion that maximizes the boundaries is of particular interest.^[29]

In addition to deposition experiments at constant potential, cyclic voltammetry (CV) studies have been performed. Previous CV studies of a variety of POPs showed a dominance of the pronounced redox behavior of the oxidized palladium(II) metal centers that get reduced concomitantly with the irreversible POP decomposition.^[30] A similar behavior was expected as well for the POP used in this work, $[\text{SrPd}_{12}\text{O}_6(\text{OH})_3(\text{PhAsO}_3)_6(\text{OAc})_3]^{4-}$

(SrPd_{12}). By steadily lowering the substrate electrode potential, the electrochemical reduction of the Pd^{II} metal centers to Pd^0 and the concurrent deposition of metallic Pd on the working electrode surface is expected to occur, while the attached ligands are stripped off and remain in solution.

Moreover, we focus in this article on the morphology of the obtained particles under reactive conditions at the verge of hydrogen evolution. Beyond this electrocatalytic application, the size-controlled deposition of Pd particles might have a larger impact in particular for specific fine-chemical syntheses: As Pd is well known to facilitate C–C coupling reactions, a systematic investigation at the solid-liquid interface is expected to give insight into the catalyst dynamics and the strong solvent influence on the reaction yield.^[31]

2. Results and Discussion

2.1. Electrochemical Reduction of SrPd_{12}

In order to investigate the deposition process in detail, a highly resolving local method is required – here, *in situ* EC-STM has been used. The $\text{Au}(111)$ support is reconstructed after preparation in flame annealing. Under potential control, this reconstruction is stable up to 0.4 V vs RHE (reversible hydrogen electrode). In order to lift the reconstruction without formation of Au adatoms, a chemical treatment in Cl^- containing solution is applied. Cl^- traces have been removed before the deposition experiments. If not stated otherwise, these experiments were performed on unreconstructed surfaces. As electrolyte for the deposition, a neutral phosphate buffer was chosen, as both the SrPd_{12} and the created nanoparticles are more stable in neutral solutions. Phosphate ions are known to form just an amorphous adlayer in neutral pH^[28] at potentials above 0.5 V vs RHE. OH^- anions, as well present in the electrolyte, are known to adsorb at potentials above 0.4 V vs RHE (see Figure S2 in the Supporting Information).^[28,32]

We started with an experiment on the unreconstructed surface in which the surface potential is subsequently lowered stepwise, starting from 0.6 V vs RHE, after adding SrPd_{12} to the phosphate buffer electrolyte. As shown in the EC-STM images acquired at different working electrode potentials in Figure 1, no deposition is observed in the potential region of 0.4 to 0.6 V vs RHE, even over a time span of 1 hour (Figure 1a). However, the SrPd_{12} gets indeed into the surface vicinity, as demonstrated by quartz microbalance measurements that indicate an increased double layer viscosity and loading upon POP addition (Figure S3). The metal deposition sets only in when lowering the potential below 0.2 V vs RHE. This potential is much lower than that of supported Pd oxide ($\text{Pd}^{\text{II}}/\text{Pd}^0$) that we determined to be around 0.7 V vs RHE in this electrolyte (see Figure 2) or to the underpotential deposition from Pd-salt precursors such as $\text{Pd}(\text{NO}_3)_2$,^[33] PdCl_2 ,^[34] and PdSO_4 from aqueous electrolytes.^[35] Although the μM SrPd_{12} concentrations used in this work are relatively low as compared to other Pd electrodeposition studies,^[26,33,36] we still see immediate deposition of small single-layer-high particles when the surface potential is set below

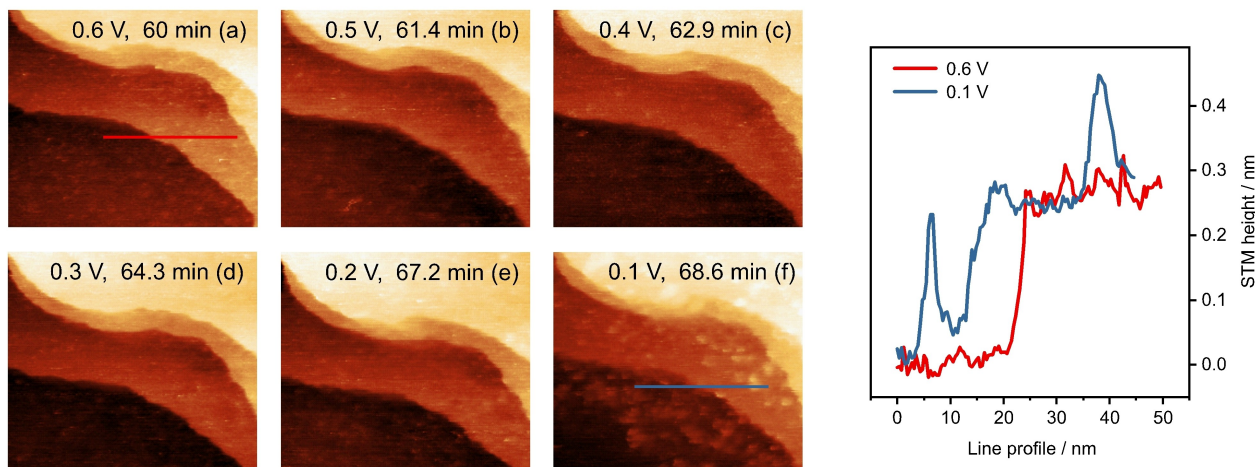


Figure 1. In situ EC-STM images (a-f) of the deposition of Pd clusters from the SrPd_{12} precursor solution by lowering the Au(111) working electrode surface potential in subsequent potentiostatic steps; particles evolve at potentials below 0.2 V vs RHE. The 50 nm horizontal profiles (right) corresponding to the lines in (a) and (f), which indicate the successful deposition of small single-layer-high Pd clusters. Imaging conditions: a-e) $U_b = -100$ mV; f) $U_b = -200$ mV, $I_t = 0.7$ nA at the indicated working electrode surface potentials. Image size: 90×80 nm 2 . Concentration: 0.3 μM SrPd_{12} in phosphate buffer (total amount corresponding to 1.1 Pd-monolayers).

0.2 V vs RHE, which indicates that sufficient amounts of SrPd_{12} precursor are present near the surface.

As observed in the line profiles of Figure 1, the deposited particles have an apparent height that corresponds to that of a monoatomic step of the Au(111) surface, in line for two materials of similar lattice constants. This height should not be influenced by the presence of residual POP-ligands or Sr^{II} ions that are all expected to be released into solution during deposition. This is evidenced by XPS spectra of the working electrode after rinsing with water and transferring to UHV (see Figure S4) where As and Sr are absent. Detailed Au 4d_{5/2} spectra (Figure S5) evidence the presence of a Pd 3d_{1/2} shoulder. This shoulder indicates the presence of metallic Pd.

For comparison, arrows pinpoint the Pd 3d_{1/2} energy position of Pd^{2+} and Pd^{4+} species, respectively. The deconvolution of the overlapping Au 4d_{5/2} and Pd 3d core level peaks can be performed, but does not lead to precise peak intensity values. Instead, the Pd MVV Auger electron yield is used to quantify the amount of deposited Pd particles (see Figure S6) confirming that the particles resolved in EC-STM entirely consist of Pd.

The low POP reduction potential compared to that of single Pd ions could be caused by thermodynamic, as well as by kinetic effects. The ligand structure around the oxygen-bridged Pd core in SrPd_{12} will shift the standard electrode potential of the $\text{Pd}^{II}/\text{Pd}^0$ couple. Furthermore, an overpotential could arise from reorganization energy contributions linked to the ligand removal upon reduction or limited electron transfer through the ligand shell.

We exclude that the SrPd_{12} deposition is related to local changes in the pH that cause their decomposition outside neutral conditions. It has been shown that only minimal pH gradients would appear near the working electrode in similarly buffered phosphate electrolytes, especially near the pK_a point

where our experiments were performed (resulting in pH differences < 1).^[37]

In order to further understand the reduction mechanism, cyclic voltammetry (CV) has been performed. Figure 2(a) shows the reduction behavior of the SrPd_{12} precursor on an Au(111) surface. The deposition cycle (red) was started at a potential where little POP is oxidized but above the PdO_x reduction. As no PdO_x reduction feature is visible, the SrPd_{12} is not yet decomposed so far. At potentials below 0.3 V vs RHE, the electrochemical SrPd_{12} reduction appears in the form of a broad peak. This reduction step yields metallic Pd particles, which matches well with the H ad-, absorption, and evolution features on Pd observed thereafter.^[38] The lower vertex potential overlaps with the onset of the hydrogen evolution reaction (HER), therefore we expect further SrPd_{12} precursors reduction in the solution, leading to less specific, additional Pd deposition. Such processes lead e.g. to the formation of Pd black when purging a SrPd_{12} solution with hydrogen gas (see Figure S7). Continuing with the anodic sweep of the CV, we observe hydrogen desorption from the Pd particles at 0.2 V vs RHE and oxidation of the metallic Pd particles at 0.9 V vs RHE. After exchanging the electrolyte to remove SrPd_{12} precursors in the solution, the CV measurement is repeated and indeed the PdO_x is reduced at 0.7 V vs RHE.

Figure 2b describes the electrochemical behavior observed when cycling towards higher, oxidizing potentials, starting from near OCP conditions. Since the SrPd_{12} ions are negatively charged, they are attracted to the surface at anodic potentials and can undergo an oxidation process. Most likely, the ligands are oxidatively separated and bare PdO_x is deposited. The known phosphate adlayer observed at these potentials seems not to hinder this electron transfer and hence a surface blocking effect as seen for sulfate^[26] can be excluded. The presence of PdO_x manifests again in a reduction peak, here around 0.75 V vs

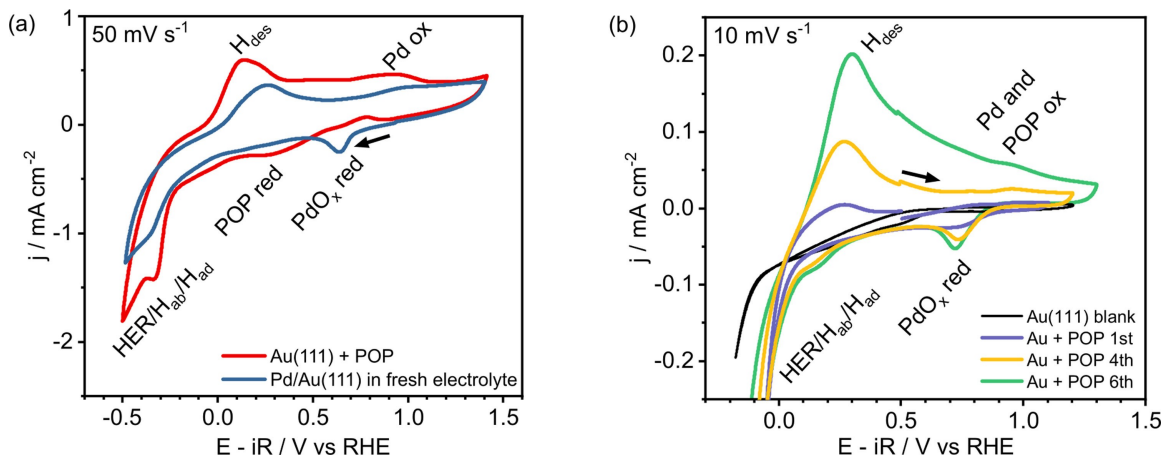


Figure 2. Cyclic voltammograms of Au(111) surfaces in a SrPd_{12} -POP solution. a) Reductive deposition process (red line) at high POP concentrations, starting from 0.9 V vs RHE directly in the cathodic direction, showing no PdO_x reduction features at 0.7 V vs RHE, but instead a broad peak at 0.2–0.3 V vs RHE, assigned to the electrochemical POP reduction. The cycle continues with entangled processes of H ad- , absorption, and evolution indicative of deposited Pd. This Pd gets oxidized in the anodic sweep at 1.0 V vs RHE. After rinsing and refilling with fresh electrolyte (blue line), a clear PdO_x reduction peak at 0.7 V vs RHE gets visible. b) Oxidative deposition process and following reduction of the PdO_x species on Au(111), starting from intermediate potential 0.5 V vs RHE, but cycling first towards higher anodic potential limits, where Pd species and deposited POPs get oxidized. The cathodic PdO_x reduction peak is now clearly visible from the first cycle on, indicative that Pd deposition has taken place at oxidizing potentials. Subsequent cycles demonstrate the ongoing deposition. Hereby, a pause of several seconds has been applied after every second cycle, in order to avoid the depletion of the SrPd_{12} precursor and to enhance the observed peaks. One CV of each pair is shown. The PdO_x reduction, H ad- , absorption, evolution, and desorption features increase with every pair of cycles and indicate the typical behavior of Pd on Au and at coverages that reach multilayer amounts. Applied concentrations: a) 10⁻³ M SrPd_{12} , pH 4 phosphate electrolyte, argon-purged; b) 10⁻³ M SrPd_{12} in pH 5.2 phosphate electrolyte, argon-purged.

RHE, that sets in already with the very first cycle, i.e. before applying the low voltages as used for the reductive deposition in Figure 2a. The PdO_x product of the oxidative deposition requires hence the same reduction potential as the supported PdO_x particles generated by reductive deposition of SrPd_{12} . The kinetic and thermodynamic barriers observed there seem no longer to apply.

The PdO_x reduction peak lowers in potential from 0.75 to 0.70 V vs RHE after stronger oxidation obtained by applying higher upper cycling potentials, a common observation for deposited Pd nanoparticles.^[39] Furthermore, the CV spectra demonstrate how the hydrogen adsorption peak develops and shifts to ~0.2 V vs RHE with increasing cycle number. However, one has to take into account that also reductive deposition takes place at these potentials, which further increases the amount of deposited Pd in the successive cycles. The small shift of the hydrogen adsorption peak has been explained with a decrease of the lateral epitaxial Pd expansion with increasing layer thickness according to the d-band model.^[40,41] We therefore deposited several ML of Pd in this experiment.

This oxidative approach promises another way to create atomically precise metal clusters, but would require a different support, since the Au(111) surface tends to roughen and form extended islands at higher potentials, which makes a distinction between Pd and Au particles hardly possible and hence prevents a detailed morphological analysis.

2.2. Resulting Particle Morphology and Dispersion

In the following, we continue with the reductive deposition, observing the initial stages of the electrochemical Pd deposition process and imaging the obtained particle morphology at high resolution by *in situ* EC-STM. As described before, the SrPd_{12} deposition requires a considerable low potentials, occurring only below 0.2 V vs RHE, where the reconstructed surface is stable. Hence no Au islands form that would act as nucleation sites for the deposition, when starting with a reconstructed surface. Even when starting with unreconstructed surfaces, the slow reconstruction kinetics keep the surface free from Au adatoms and holes, on the time scale of the deposition experiments.

As can be seen in Figure 3, a similar deposition of small particles takes place on both reconstructed and unreconstructed surface terraces, rather independent from the applied potential steps. Importantly, as shown in the inset of Figure 3a, one does not observe a preferential adsorption at step edges that would manifest in a step meandering, as observed for the small overpotential deposition of various Pd salts in different electrolytes by Köntje, et al.^[33] Instead, the low potentials applied here result in a uniform and random distribution of small Pd particles on the flat Au(111) terraces, similar to the deposition from Pd salt solutions with moderate^[42] to large overpotentials.^[26,43]

While the nucleation on terraces is similar, the central question is whether the POP deposition gives access to a better size control. When characterizing area and height distributions in Figure 3c, care has been taken to apply only rather short potentiostatic treatments, to minimize concomitant coalescence

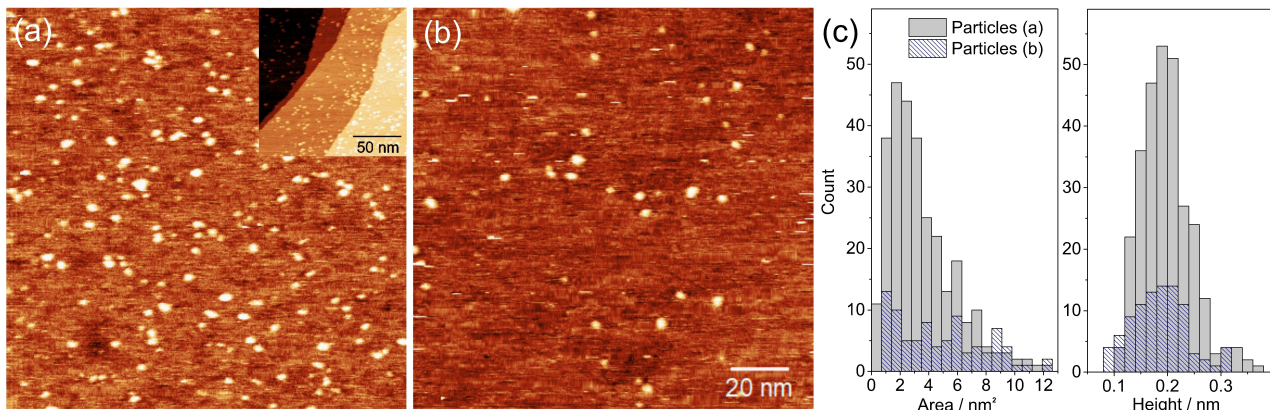


Figure 3. In situ EC-STM images of the deposition of Pd clusters from the SrPd_{12} precursor solution after two different preparation pathways: a) on unreconstructed Au(111) after 2 pulses of 500 ms at 0 V, inset: larger overview including steps with no preferential deposition; b) on reconstructed Au(111) after 3 treatments of 30 s at 0.2 V vs RHE. The faint parallel lines observed on certain parts of the surface indicate the presence of the herringbone reconstruction. c) Corresponding histograms of particle area and height. The clusters are almost exclusively one atomic layer high and show an area dispersion that starts with areas compatible to those observed for supported Pd_{12} clusters in UHV (apparent diameters of 2 nm, hence areas of 3 nm^2 ^[44]). The particle morphology is measured at 0.5 V vs RHE (a), resp. 0.4 V vs RHE (b) surface potential. Imaging conditions: a) $U_b = -150 \text{ mV}$, $I_t = 2 \text{ nA}$. b) $U_b = -28 \text{ mV}$, $I_t = 0.35 \text{ nA}$. Concentration: 0.1 μM SrPd_{12} in phosphate buffer (total amount corresponding to 0.5 Pd-monolayers).

and alloying with Au adatoms. Two recipes have been used: In Figure 3a, two short pulses of 500 ms at a low potential of 0.0 V vs RHE lead to a coverage of about 5%, as determined by the observed surface area, while in Figure 3b three longer treatments of 30 s at a less negative potential of 0.2 V vs RHE lead to a lower coverage of about 2%.

With both treatments, we observe similar distributions. In particular, both led almost exclusively to single-layer-high particles ($\geq 95\%$) with an apparent height of about 0.2 nm. This is in line with an expected epitaxial growth, as seen in most previous studies,^[26,33] except for the very slow deposition in highly dilute electrolytes on the reconstructed surface by Uosaki et al., in which 3D particles up to three layers high have been found.^[27] Note that different tip radii might slightly influence the observed area, but not the observed height distributions.

Remarkably, the prevalent observed particle areas at the small-size-onset are roughly 2.0 (a), resp. 1.5 nm^2 (b), corresponding to an average particle diameter of 1.4 to 1.6 nm. This apparent average diameter, enlarged by tip convolution effects, fits well the size observed for one single-layer-high Pd_{12} clusters supported on a boron nitride support by STM under vacuum conditions.^[44] The two area histograms show distinct differences: the higher coverage histogram in (a), obtained by short potential pulses, is peaked at smaller cluster areas, while the histogram in (b), obtained by much longer potential treatments, is somewhat broader. Shorter deposition times seem therefore beneficial for the formation of small, size-controlled clusters, although the limited set of experiments makes it difficult to assign these to single, specific parameters. The histogram related to (b) shows furthermore indications for a peak sequence with about 2 nm^2 distance. This could be related to a preferential deposition close to already deposited Pd_{12} units, especially if the deposition is slow enough to overcome transport limitations. That the high coverage sample (a) does not show such a peak series, might be related to an enhanced

ripening due to a higher particle coverage. For future deposition strategies, it might be helpful to deposit metal clusters from neutral^[45] or positively charged POPs that do not get repelled from the surface upon reduction, instead of the strongly negatively charged one used here. This could be easily feasible as the potential of zero charge of Au(111) in phosphate electrolyte is around 0.6 V vs RHE.^[46]

2.3. Hydrogen-Induced Deposition of SrPd_{12}

Due to the low potentials required, the electrochemical SrPd_{12} deposition takes place in a potential region where hydrogen adsorption starts to take place, especially once first traces of Pd have been deposited. This adsorption occurs already well before hydrogen evolution sets in (at potentials that depend strongly on the preparation conditions, about -0.1 V vs RHE on bare Au(111), 0.0 V vs RHE on Pd films, see Figure 2). In order to better understand how hydrogen formation and the presence of adsorbed hydrogen might modify the deposition, we performed several experiments described in the following.

We started with studying the SrPd_{12} deposition on an HOPG support, where the blank surface, contrary to Au(111), does not develop hydrogen at all in the investigated potential range, as seen in Figure S8. Upon POP addition and cycling, however, hydrogen adsorption and evolution can be seen as well. Hence Pd deposition must have taken place and occurred, at least initially, without the presence of adsorbed hydrogen. Later on, an intricate entanglement of deposition and hydrogen evolution is evidenced by the observed crossing of the CV currents at low potentials in the first two cycles. This points to a hydrogen-induced deposition of new active sites for hydrogen evolution during the voltage sweep. These consist of increasing amounts of deposited Pd^0 that shifts the hydrogen adsorption and evolution potentials towards more positive values in the second

and third cycle, until the shoulder at 0.2 V vs RHE appears as observed for Pd/Au(111). Due to the limited interaction between Pd cluster and the HOPG terraces, the cluster aggregate upon deposition, mostly at step edges, and the size distribution is lost.

From our hydrogen purging experiments we know on the other hand, as already mentioned, that the SrPd_{12} polyanions are unstable in the presence of hydrogen gas – an instant formation of black Pd aggregates is observed in solution (Figure S7). Such an effect has already been exploited for the wet-chemical synthesis of large Pd aggregates with sizes around 8 nm by reduction of heteropolytungstates containing 1 or 2 Pd^{II} ions.^[47] We can therefore anticipate that this chemical reduction mechanism, in parallel to the electrochemical one, leads to the formation of particles with higher aggregation probability, lowering the size-control.

In order to get a closer insight via EC-STM measurements, we tried out different pretreatments of the solid-liquid interface at low potentials, where adsorbed hydrogen forms, at the verge of hydrogen evolution. These hydrogen species are not imaged by EC-STM, but have a strong impact on the Pd deposition when subsequently adding the POP, SrPd_{12} , at a surface potential of 0.3 V vs RHE or higher, where no deposition would occur in a pristine solution, even after a prolonged time of more than one hour (as demonstrated in Figure 1). The pretreatments consisted in (i) keeping the Au(111) surface at 0.1 V vs RHE for 90 min (result shown in Figure 4a) or (ii) at a lower potential of 0.0 V vs RHE for a shorter time of 10 min (result shown in Figure 4b) or (iii) after applying 6 × 500 ms potential steps at −0.1 V vs RHE and waiting for about 20 min (result shown in Figure S9). We then added SrPd_{12} and indeed, a spontaneous Pd particle deposition is observed that leads to completely different, large, flower-like aggregates shown in Figure 4.

This spontaneous deposition happens within a timeframe of less than five minutes, as these structures appear already in the very first acquired image and do not change thereafter in size or shape. The flower-like particles are randomly distributed, though a preferential attachment to step edges is observed. The apparent island shape in Figure 4a,b (left) depends strongly on the tip quality. Sometimes, one can still recognize voids and a strong height heterogeneity within the prevalently single-layer-high islands – this points to structures that form by a hit-and-stick aggregation followed by an only partial coalescence.

The process ends probably due to the consumption of a chemical species present at the solid-liquid interface and/or the electrolyte. This limiting species is not surface-near SrPd_{12} , even if only very small concentrations were used, corresponding to just 1.6 equivalent Pd monolayers that can be deposited at maximum: When lowering the surface potential again, the particle deposition as described earlier resumes. As shown in Figures 4a (right) and in Figure S9, further small Pd particles of an average equivalent diameter of 2.5 ± 0.9 nm are deposited from the same solution. Those small spherical particles are randomly dispersed and are not preferentially deposited near the flower-like structures or step edges. The small particles

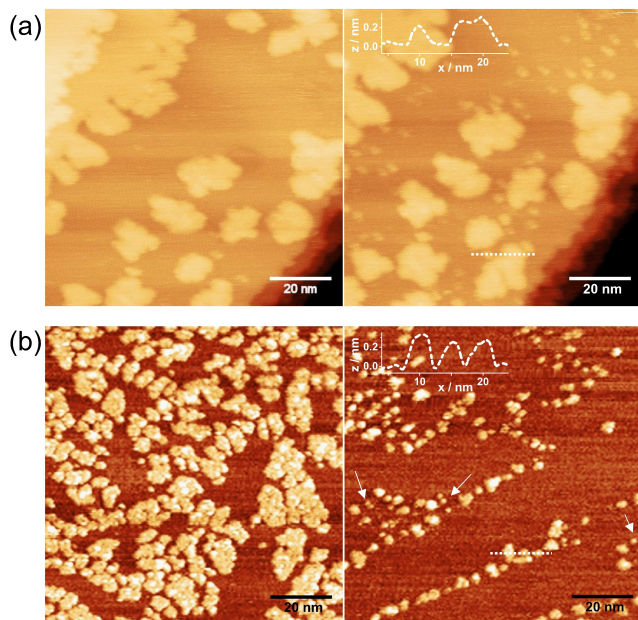


Figure 4. *In situ* EC-STM images indicating the formation of larger, flower-like Pd islands of one atomic layer height after different pretreatments of the solid-liquid interface at low potentials before addition of SrPd_{12} . Under these pretreatments, hydrogen species are formed. Experiment series (a): Aggregates appearing after keeping the surface for 90 min at 0.1 V vs RHE and sequentially adding SrPd_{12} precursor at a surface potential of 0.3 V vs RHE, i.e. at a potential where no deposition would occur in a pristine solution (left; compare with Figure 1); when lowering the potential again to 0.1 V vs RHE without changing the solution (right), small particles can again be deposited, in addition to the already present flower-like particles. Experiment series (b): Similar effects can be obtained by keeping the surface for only 10 min at a lower potential of 0.0 V vs RHE and adding the precursor again at 0.3 V vs RHE (left); investigating a surface area kept directly under the tip (right) reveals the tip influence on local potential and transport: Less and much smaller aggregates are observed, down to sizes compatible with Pd_{12} (see arrows), decorating elbow sites. Imaging conditions: $I_t = 0.2$ nA; $U_b = -100$ mV (a, left), $U_b = -300$ mV; (a, right) $U_b = -40$ mV (b). All images have been taken at 0.3 V vs RHE working electrode surface potential. Concentration: 0.4 μM SrPd_{12} in phosphate buffer (total amount corresponding to 1.6 Pd-monolayers).

therefore correspond well to the previously described electrochemical reduction mechanism.

The limiting species is hence hydrogen-related. Its formation seems to be confined to the solid-liquid interface that gets saturated upon the pretreatment – if the hydrogen species could evolve directly into solution, it would probably accumulate in quantities that react off the entire amount of solved SrPd_{12} . However, we cannot exclude that adsorbed hydrogen leaves the Au(111) surface after going back up in potential and that the chemical reduction occurs already in solution. In any case, the aggregation indicates that the POP reduction takes place in the vicinity of the nucleation centers, either directly by adsorbed hydrogen or from hydrogen in solution.

The influence of present hydrogen species on the Pd particle deposition was also stressed by previous investigations with EC-STM^[43] and *in situ* TEM^[48] that observed the formation of rough porous aggregates when applying potentials where hydrogen forms on the surface. They attributed the changes in

morphology to a competition for direct surface access between adsorbed hydrogen and the Pd precursor.

While usually the deposition was performed with a retracted tip, the experiment in Figure 4b explicitly addresses the influence of the tip during the deposition process. The left image displays the particle distribution when the tip was distant, the right one the distribution directly under the tip. One observes immediately that much less and smaller clusters have been deposited. The integrated area that is covered by Pd particles decreases by a factor of four. For Pd deposition on Au(111) from salt solutions, such a tip shielding effect was already hypothesized by Naohara, et al.^[43] who suggested a precursor diffusion limitation to be responsible for a reduced deposition directly under the tip. Such transport limitation, by electrostatic and geometric shielding, will be even more important for large and four times negatively charged precursors such as the **SrPd₁₂**. In these experiments, the tip potential was constantly kept at 0.35 V vs RHE, also during the 10 min of 0 V vs RHE. This tip potential could also affect the local working potential of the surface under the tip, locally changing the effect of pretreatment and subsequent deposition.

Noticeably, at the low coverage of particles forming under the tip, we can observe a distinct preference for specific nucleation sites. As this deposition took place on a reconstructed Au(111) surface, we attribute the line order to the presence of elbow sites of the herringbone structure where nucleation is favored, as reported for UHV vapor deposited^[49,50] or electrochemically deposited Pd particles on reconstructed Au(111).^[27] The preference for defect sites and steps after hydrogen preconditioning underlines a considerable mobility of

the particles forming in the deposition process, in line with the observed tendency to aggregate.

All the mechanistic considerations regarding chemical and electrochemical reductive deposition of **SrPd₁₂** up to now demonstrate the importance of a rational control of the surface potential before and during the deposition process for obtaining size-selected particles. In addition, an even better control could be gained at higher pH to further reduce the hydrogen production while remaining in the POP stability window.

2.4. Morphology Changes under Reaction Conditions

If the presence of adsorbed hydrogen changes the POP deposition dramatically, the question arises how stable the deposited particles are, once formed, under HER conditions. Since the XPS measurements suggested that the Pd particles are metallic, it is interesting to see whether they show the characteristic hydrogen adsorption signatures in STM. To that purpose we investigated the morphology *in situ*, in a fresh electrolyte, at low potentials. After the particle deposition (preparation as in Figure 3a), the reactor cell was thoroughly rinsed and refilled with pure phosphate buffer solution, in order to remove all non-reacted **SrPd₁₂**, while keeping the sample under potential control at 0.6 V vs RHE. The surface potential was then, in single potentiostatic steps, lowered to 0.0 V vs RHE and back to 0.6 V vs RHE for two consecutive cycles while being imaged by EC-STM (Figure 5).

A clear swelling of the Pd clusters is observed when lowering the electrochemical potential (Figures 5b, 5g). The shift in the height histogram in Figure 5d indicates an increase

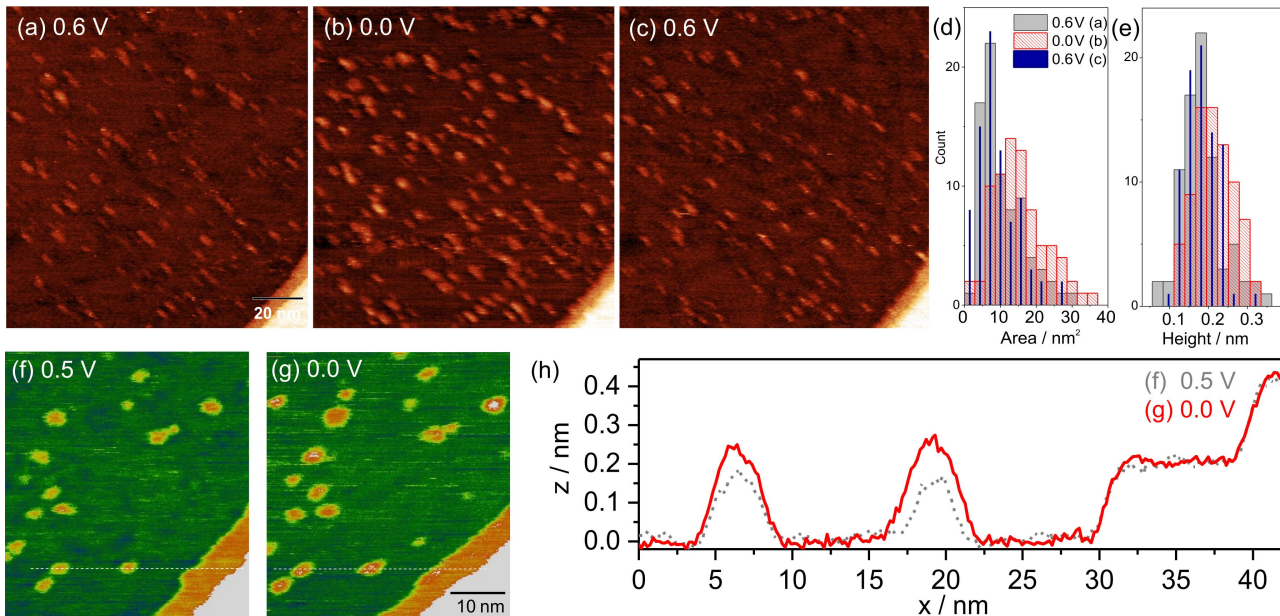


Figure 5. *In situ* EC-STM images indicating the influence of the surface potential on the apparent Pd particle morphology at the onset of hydrogen evolution: a-c) Images taken at indicated surface potentials; d, e) corresponding histograms of apparent particle area and height indicate a reversible increase of both at low potentials. f,g) Zoom images on potential-dependent particle morphology during a second potential cycle taken at indicated surface potentials. h) Corresponding line profile (dotted lines in f and g) indicates that only the Pd particle morphology changes while Au step edges remain unchanged. Imaging conditions: $I_t = 2 \text{ nA}$, tip potential kept at 0.65 V vs RHE. Concentration: 0.1 μM **SrPd₁₂** in phosphate buffer (total amount corresponding to 0.5 Pd-monolayers).

by roughly 20%. This change in height concerns only the deposited Pd particles and not the Au support, as is clearly visible in the potential-dependent line profiles in Figure 5h. This points to the more active nature of the deposited Pd particles and rules out a tip-induced effect. Concomitantly, the apparent area increases by 70%, but, contrary to the straightforward height evaluation, this increase depends strongly on the threshold values used for the cluster area detection and might mostly be induced by a tip convolution effect linked to the height increase.

The swelling effect is reversible, as can be seen in Figure 5c. Since the corresponding histograms largely overlap with the initial ones, it is only a minute fraction of particles that undergoes ripening or irreversible changes. Such swelling of Pd particles has been observed before, on a Pt(111) support^[51] and was attributed to hydrogen ad- and absorption into the Pd adlayer. Absorption, i.e. uptake into the bulk, can be excluded in our case, as the particles are just 1 ML in height and hydrogen absorption on Pd/Au(111) has been shown by Baldauf et al. to take only place starting from 2 ML.^[52] The apparent height increase related to hydrogen adsorption might thus be explained by an electronic effect, i.e. an adsorbate-induced change in the electronic density of states.

Hydrogen-induced coalescence is only sporadically observed in these experiments, most particles do not ripen even at very close distance. We conclude that the particles, once formed, are stable under HER conditions, in contrast to the **SrPd₁₂** precursors that decompose under these conditions. In addition, the particles show indeed the same characteristic hydrogen adsorption signatures in the STM images at different surface potentials that are found for metallic Pd nanostructures deposited from salt solutions.

3. Conclusions

This study investigates by EC-STM a novel Pd cluster preparation technique on Au(111) where size-controlled particles are deposited by reduction of **SrPd₁₂** precursors. This reduction occurs at potentials below 0.2 V vs RHE and requires potentials lower by roughly 0.5 V, compared to the reduction of bare PdO_x particles in the same electrolyte, due to thermodynamic and kinetic effects related to the extended, complex **SrPd₁₂**-ligand shell. Besides the deposition by reductive decomposition, also an oxidative approach is investigated, in which deposition occurs via ligand removal prior to a subsequent Pd oxide reduction. Single-layer-high Pd clusters resulting from the reductive approach could be imaged *in situ* and show a very narrow size distribution, as long as low concentrations and short deposition times are applied.

Besides the electrochemical reduction, an alternative deposition route is observed, if hydrogen intermediates are present on the surface. This later route leads to large, flower-like Pd islands. Hydrogen-induced effects on the onset of the reduction in the electrochemical route can be excluded by deposition experiments on an HER-inert HOPG surface. Finally, the deposited small Pd clusters were studied at potentials around

the onset of HER, where they behave similar to metallic Pd nanostructures that increase in apparent area and height due to hydrogen absorption.

This study paves therefore the way to deposit size-controlled Pd clusters for more systematic studies on size effects in cluster catalysis at the solid-liquid interface.

Experimental Section

All materials in contact with the electrolyte and sample like glassware and PEEK sample holder were cleaned with Caro's acid followed by rinsing at least three times with boiling ultrapure water. Unless stated otherwise a neutral 0.05 M phosphate buffer electrolyte was used, which was prepared from ultrapure water (18.2 MΩ), H₃PO₄ (Suprapur, Merck), and NaOH (monohydrate, 99.99%, Merck) with a pH of 6. The **SrPd₁₂** stock solution (0.2 g/L) is made in the same electrolyte and added during the experiment as indicated.

Cylindrically shaped Au(111) single crystals (Ø 8 or 10 mm, MaTeck) were used as substrates and cleaned prior to each experiment by oxidation in 3 M H₂SO₄ (Suprapur, Merck) until the formation of a reddish layer, which was removed with 6 M HCl. Subsequently, they were flame-annealed with a hydrogen flame at red heat for two minutes and slowly cooled down in high-purity argon atmosphere leading to the reconstructed Au(111)(22×√3) surface. As the reconstructions already lifts at the open circuit potential, it is important to control the potential prior to the insertion of the gold sample. The unreconstructed Au(111)(1×1) surface is prepared as the reconstructed surface, but followed by an additional 30 min immersion into a 0.05 M potassium chloride solution.

The HOPG sample (7×7×0.6 mm, NT-MDT) was freshly cleaved with scotch tape prior mounting in the sample holder.

The integral electrochemical methods were performed with an ECi200 potentiostat from Nordic Electrochemistry Aps. A platinum wire (MaTeck, 99.9%, Ø 0.8 mm) was used as counter electrode. As reference electrode freshly prepared reversible hydrogen electrode or Ag/AgCl (Science Line, SI Analytics) were used as reference electrode. For comparability, all potentials have been converted to values referenced to a reversible hydrogen electrode (RHE). The measurements were corrected for ohmic drop measured by the potentiostat after the measurement if stated in the figure.

All EC-STM experiments have been performed with an EC-STM, developed by Wilms, et al.^[53] and equipped with an SPM100 electronics (RHK Technology Inc.) for imaging. The electrochemical potential control of the studied surface is enabled through a Picostat potentiostat (Molecular Imaging Inc.). In this work, all mentioned tip and surface potentials are referenced versus the reference electrode. To this purpose, platinum wires (MaTeck, 99.9%, Ø 0.8 mm) were used as both, counter, and pseudo reference electrode, but the potentials were converted to values referenced to a RHE. The Ir/Pt tips were prepared by mechanical cutting or electrochemical etching in KOH/KSCN solution. In order to reduce overlaying faradaic currents, the majority of the tip, except for the apex, was coated with Apiezon wax. The remaining tip area exposed to the electrolyte was controlled prior the experiment by the measurement of the tip leakage current, while being in the electrolyte and not in tunneling condition. Usually tips showed a leakage current below 30 pA. The samples were fixed in a PEEK sample holder and contacted from the backside. STM images were analyzed by the Gwyddion software^[54] with a line-by-line linear background subtraction. The apparent height was referenced to the average background height of the terraces and the height

scale calibrated for Au(111) steps (0.24 nm). Line profiles were taken horizontally in the fast scanning direction in order to minimize the effect of drift.

Acknowledgements

The authors would like to thank Dr. Hany El-Sayed and Dr. habil Oliver Schneider for the discussion and valuable comments, which helped to improve this work and Dr. Gustav Wiberg for the support with the potentiostatic measurements. F.E. and N.B. acknowledge support by the German Research Council (DFG, through project ES 349/4-1 and TUM International Graduate School of Science and Engineering, IGSSE). A.D.C. thanks the financial support by the Alexander von Humboldt Foundation. U.K. thanks the German Research Council (DFG, KO-2288/26-1), Jacobs University, and CMST COST Action CM1203 (PoCheMoN) for support. T.M. acknowledges China Scholarship Council (CSC) for a doctoral fellowship. Open access funding enabled and organized by Projekt DEAL.

Conflict of Interest

The authors declare no conflict of interest.

Keywords: electrodeposition • electrochemical scanning tunneling microscopy • cluster • polyoxometalates • palladium

- [1] T. Naito, T. Shinagawa, T. Nishimoto, K. Takanabe, *ChemSusChem* **2020**, *13*, 5921–5933.
- [2] B. R. Cuenya, *Thin Solid Films* **2010**, *518*, 3127–3150.
- [3] S. Kunz, K. Hartl, M. Nesselberger, F. F. Schweinberger, G. Kwon, M. Hanzlik, K. J. Mayrhofer, U. Heiz, M. Arenz, *Phys. Chem. Chem. Phys.* **2010**, *12*, 10288–10291.
- [4] M. Nesselberger, M. Roefzaad, R. F. Hamou, P. U. Biedermann, F. F. Schweinberger, S. Kunz, K. Schloegl, G. K. Wiberg, S. Ashton, U. Heiz, K. J. Mayrhofer, M. Arenz, *Nat. Mater.* **2013**, *12*, 919–924.
- [5] G. Kwon, G. A. Ferguson, C. J. Heard, E. C. Tyo, C. Yin, J. DeBartolo, S. Seifert, R. E. Winans, A. J. Kropf, J. Greeley, R. L. Johnston, L. A. Curtiss, M. J. Pellin, S. Vajda, *ACS Nano* **2013**, *7*, 5808–5817.
- [6] A. von Weber, S. L. Anderson, *Acc. Chem. Res.* **2016**, *49*, 2632–2639.
- [7] T. Imaoka, Y. Akanuma, N. Haruta, S. Tsuchiya, K. Ishihara, T. Okayasu, W. J. Chun, M. Takahashi, K. Yamamoto, *Nat. Commun.* **2017**, *8*, 688.
- [8] W. W. Ayass, J. F. Minambres, P. Yang, T. Ma, Z. Lin, R. Meyer, H. Jaensch, A. J. Bons, U. Kortz, *Inorg. Chem.* **2019**, *58*, 5576–5582.
- [9] S. Bhattacharya, W. W. Ayass, D. H. Taffa, A. Schneemann, A. L. Semrau, S. Wannapaiboon, P. J. Altmann, A. Pothig, T. Nisar, T. Balster, N. C. Burch, V. Wagner, R. A. Fischer, M. Wark, U. Kortz, *J. Am. Chem. Soc.* **2019**, *141*, 3385–3389.
- [10] S. Bhattacharya, W. W. Ayass, D. H. Taffa, T. Nisar, T. Balster, A. Hartwig, V. Wagner, M. Wark, U. Kortz, *Inorg. Chem.* **2020**, *59*, 10512–10521.
- [11] V. Kogan, Z. Aizenshtat, R. Popovitz-Biro, R. Neumann, *Org. Lett.* **2002**, *4*, 3529–3532.
- [12] P. Losch, W. X. Huang, E. D. Goodman, C. J. Wrasman, A. Holm, A. R. Riscoe, J. A. Schwalbe, M. Cargnello, *Nano Today* **2019**, *24*, 15–47.
- [13] T. Imaoka, H. Kitazawa, W. J. Chun, S. Omura, K. Albrecht, K. Yamamoto, *J. Am. Chem. Soc.* **2013**, *135*, 13089–13095.
- [14] L. R. Merte, F. Behafarid, D. J. Miller, D. Friebel, S. Cho, F. Mbuga, D. Sokaras, R. Alonso-Mori, T. C. Weng, D. Nordlund, A. Nilsson, B. Roldan Cuenya, *ACS Catal.* **2012**, *2*, 2371–2376.
- [15] X. K. Wan, H. B. Wu, B. Y. Guan, D. Luan, X. W. D. Lou, *Adv. Mater.* **2020**, *32*, e1901349.
- [16] P. Yang, U. Kortz, *Acc. Chem. Res.* **2018**, *51*, 1599–1608.
- [17] P. Yang, Y. Xiang, Z. Lin, B. S. Bassil, J. Cao, L. Fan, Y. Fan, M. X. Li, P. Jimenez-Lozano, J. J. Carbo, J. M. Poblet, U. Kortz, *Angew. Chem. Int. Ed.* **2014**, *53*, 11974–11978; *Angew. Chem.* **2014**, *126*, 12168–12172.
- [18] L. H. Bi, M. Reicke, U. Kortz, B. Keita, L. Nadjo, R. J. Clark, *Inorg. Chem.* **2004**, *43*, 3915–3920.
- [19] E. V. Chubarova, M. H. Dickman, B. Keita, L. Nadjo, F. Misquer, M. Mifsud, I. W. Arends, U. Kortz, *Angew. Chem. Int. Ed.* **2008**, *47*, 9542–9546; *Angew. Chem.* **2008**, *120*, 9685–9689.
- [20] N. V. Izarova, R. N. Biboum, B. Keita, M. Mifsud, I. W. Arends, G. B. Jameson, U. Kortz, *Dalton Trans.* **2009**, 9385–9387.
- [21] M. Barsukova, N. V. Izarova, R. N. Biboum, B. Keita, L. Nadjo, V. Ramachandran, N. S. Dalal, N. S. Antonova, J. J. Carbo, J. M. Poblet, U. Kortz, *Chem. Eur. J.* **2010**, *16*, 9076–9085.
- [22] J. Friedl, R. Al-Oweini, M. Herpich, B. Keita, U. Kortz, U. Stimming, *Electrochim. Acta* **2014**, *141*, 357–366.
- [23] M. Ammam, B. Keita, L. Nadjo, I.-M. Mbomekalle, M. D. Ritorto, T. M. Anderson, W. A. Neiwert, C. L. Hill, J. Fransaer, *Electroanalysis* **2011**, *23*, 1427–1434.
- [24] G. E. Engelmann, J. C. Ziegler, D. M. Kolb, *J. Electrochem. Soc.* **1998**, *145*, L33–L35.
- [25] J. Meier, J. Schiotz, P. Liu, J. K. Norskov, U. Stimming, *Chem. Phys. Lett.* **2004**, *390*, 440–444.
- [26] S. Pandelov, U. Stimming, *Electrochim. Acta* **2007**, *52*, 5548–5555.
- [27] S. Takakusagi, K. Kitamura, K. Uosaki, *Electrochim. Acta* **2009**, *54*, 5137–5141.
- [28] A. Cuesta, M. Kleinert, D. M. Kolb, *Phys. Chem. Chem. Phys.* **2000**, *2*, 5684–5690.
- [29] J. H. K. Pfisterer, Y. Liang, O. Schneider, A. S. Bandarenka, *Nature* **2017**, *549*, 74–77.
- [30] M. Barsukova-Stuckart, N. V. Izarova, R. A. Barrett, Z. Wang, J. van Tol, H. W. Kroto, N. S. Dalal, P. Jimenez-Lozano, J. J. Carbo, J. M. Poblet, M. S. von Gernler, T. Drewello, P. de Oliveira, B. Keita, U. Kortz, *Inorg. Chem.* **2012**, *51*, 13214–13228.
- [31] J. Sherwood, J. H. Clark, I. J. S. Fairlamb, J. M. Slattery, *Green Chem.* **2019**, *21*, 2164–2213.
- [32] A. C. Chen, J. Lipkowski, *J. Phys. Chem. B* **1999**, *103*, 682–691.
- [33] C. Köntje, L. A. Kibler, D. M. Kolb, *Electrochim. Acta* **2009**, *54*, 3830–3834.
- [34] L. A. Kibler, A. M. El-Aziz, D. M. Kolb, *J. Mol. Catal. A* **2003**, *199*, 57–63.
- [35] J. Tang, M. Petri, L. A. Kibler, D. M. Kolb, *Electrochim. Acta* **2005**, *51*, 125–132.
- [36] M. E. Björketun, G. S. Karlberg, J. Rossmeisl, I. Chorkendorff, H. Wollschmidt, U. Stimming, J. K. Nørskov, *Phys. Rev. B* **2011**, *84*.
- [37] K. Obata, L. Stegenburga, K. Takanabe, *J. Phys. Chem. C* **2019**, *123*, 21554–21563.
- [38] W. B. Ju, T. Brulle, M. Favaro, L. Perini, C. Durante, O. Schneider, U. Stimming, *ChemElectroChem* **2015**, *2*, 547–558.
- [39] V. C. Diculescu, A. M. Chiorcea-Paquin, O. Corduneanu, A. M. Oliveira-Brett, *J. Solid State Electrochem.* **2007**, *11*, 887–898.
- [40] L. A. Kibler, *ChemPhysChem* **2006**, *7*, 985–991.
- [41] B. Hammer, J. K. Norskov, *Surf. Sci.* **1995**, *343*, 211–220.
- [42] H. Naohara, S. Ye, K. Uosaki, *J. Phys. Chem. B* **1998**, *102*, 4366–4373.
- [43] H. Naohara, S. Ye, K. Uosaki, *Colloids Surf. A* **1999**, *154*, 201–208.
- [44] B. Wang, B. Yoon, M. Konig, Y. Fukamori, F. Esch, U. Heiz, U. Landman, *Nano Lett.* **2012**, *12*, 5907–5912.
- [45] S. Bhattacharya, U. Basu, M. Haouas, P. Su, M. F. Espenship, F. Wang, A. Sole-Daura, D. H. Taffa, M. Wark, J. M. Poblet, J. Laskin, E. Cadot, U. Kortz, *Angew. Chem. Int. Ed.* **2021**, *60*, 3632–3639.
- [46] Z. Su, J. Leitch, J. Lipkowski, *Z. Phys. Chem.* **2012**, *226*, 995–1009.
- [47] R. Villanneau, A. Roucoux, P. Beaunier, D. Brouxi, A. Proust, *RSC Adv.* **2014**, *4*, 26491–26498.
- [48] J. Yang, C. M. Andrei, Y. Chan, B. L. Mehdi, N. D. Browning, G. A. Botton, L. Soleymani, *Langmuir* **2019**, *35*, 862–869.
- [49] C. Wu, F. Xu, M. R. Castell, S. C. Tsang, *Chem. Commun. (Camb.)* **2014**, *50*, 1198–1201.
- [50] C. J. Baddeley, R. M. Ormerod, A. W. Stephenson, R. M. Lambert, *J. Phys. Chem.* **1995**, *99*, 5146–5151.
- [51] J. A. Mwanda, A. Cuesta, *Electrochim. Acta* **2018**, *292*, 419–424.
- [52] M. Baldauf, D. M. Kolb, *Electrochim. Acta* **1993**, *38*, 2145–2153.
- [53] M. Wilms, M. Krift, G. Bermes, K. Wandelt, *Rev. Sci. Instrum.* **1999**, *70*, 3641–3650.
- [54] D. Nečas, P. Klapetek, *Open Phys.* **2012**, *10*, 181–188.

Manuscript received: January 28, 2021

Revised manuscript received: February 17, 2021

Accepted manuscript online: February 17, 2021